Science Advances
AAAS

Supplementary Materials for

Unprecedented accuracy in molecular line-intensity ratios from frequency-based measurements

Jin-Ke Li *et al.*

Corresponding author: Yan Tan, tanyan@ustc.edu.cn; Jonathan Tennyson, j.tennyson@ucl.ac.uk;
Shui-Ming Hu, smhu@ustc.edu.cn

Sci. Adv. **11**, eadz6560 (2025)
DOI: 10.1126/sciadv.adz6560

This PDF file includes:

S1 Experimental Line-intensity ratios

Experimental Method

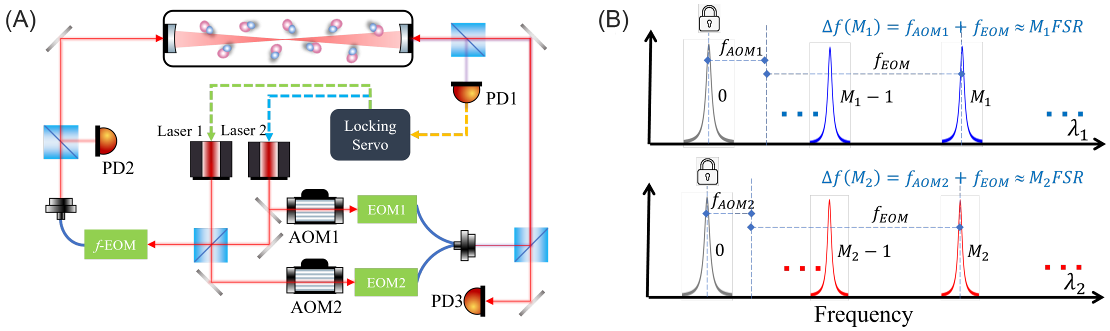

Figure S1: **DW-CMDS schematic and mode squeezing concept.** (A) Configuration of the experimental setup for dual-wavelength cavity mode dispersion spectroscopy (DW-CMDS). (B) Resonance condition of the probe beams. Abbreviations: AOM, acousto-optic modulator; ECDL, external-cavity diode laser; EOM, electro-optic modulator; PD, photodiodes.

A schematic of the experimental setup is shown in fig. S1. Two external cavity diode lasers (ECDL, Toptica DL Pro) were used for the DW-CMDS measurements. Both lasers, operating at wavelengths λ_1 and λ_2, were locked to a high-finesse optical cavity using the Pound-Drever-Hall (PDH) technique. Two lasers were combined using a fiber optic combiner, sharing a common frequency-locking path. The optical cavity consisted of a pair of high-reflectivity (HR) mirrors (R = 99.998% at 1.5 - 1.7 μm), separated by 140 cm, corresponding to a free spectral range (FSR) of 107.282 MHz and a mode width of approximately 0.6 kHz. Different modulation frequencies (20 and 30 MHz) were applied to the lasers, allowing simultaneous PDH locking of both without interference using the same optical path. An acousto-optic modulator (AOM1/AOM2) was introduced to shift the frequency of each locking beam.

Another beam from each laser, used for spectral probing, was coupled into a fiber electro-optic modulator (EOM) and directed into the optical cavity. The resonance condition for a probing laser beam is depicted in fig. S1B. It is fulfilled when the sum of the AOM frequency (f_{AOM1} or f_{AOM2}) and the fiber-EOM frequency (f_{EOM}) equals the frequency shift of a cavity mode ($\Delta f(M_1)$ or

$\Delta f(M_2)$) from the locking mode.

$$f_{A1} + f_E = \Delta f(M_1) \approx M_1\mathrm{FSR} \qquad @\lambda_1; \tag{S1}$$

$$f_{A2} + f_E = \Delta f(M_2) \approx M_2\mathrm{FSR} \qquad @\lambda_2; \tag{S2}$$

As the AOM frequencies differ from the cavity's FSR, only one sideband of one probing beam meets the resonance condition at a given fiber-EOM modulation frequency. By scanning the EOM frequency and detecting the transmitted light power with a photodetector (PD1), we precisely determined the frequency shifts in the cavity modes due to the molecular absorption. Two sets of frequency shifts at both wavelengths were measured within a single spectral scan, which took approximately 10 seconds. Displayed in fig. S2 is a sample CMDS spectrum of the P(5) line (upper panel) together with transmittance spectra at two different cavity modes, one on the baseline far from the molecular absorption line P(5) center and the other one close to P(5) center.

The power of the locking lasers before entering the cavity was about 0.1 mW, while the power of the probe lasers was approximately 2 mW. Note that the probe light was modulated by a fiber-EOM, and the carrier was not resonant with the cavity mode. The sidebands that were resonant with the cavity mode accounted for approximately 1/3 of the total power. Spectra were acquired by scanning the sidebands of the f-EOM. Each measurement captured a pair of spectral lines simultaneously and took about 10 seconds to complete. The signal-to-noise ratio (SNR) of a single spectrum was approximately 2000:1.

The aluminum cavity cylinder was temperature-stabilized using a locking servo. After the cavity temperature was stabilized, the measured temperature ranged between 298.41 K and 298.43 K. The temperature of the resonant cavity was monitored using two calibrated platinum resistance thermometers, which were in good contact with the cavity walls. These thermometers were positioned at both ends of the cavity, and their readings were recorded using an MKT50 device from Anton Parr. The sensors have been calibrated at the triple points of water and gallium, with an uncertainty of ±5 mK. After filling the gas sample into the cavity, a stabilization period of at least 20 minutes was taken before measurements to ensure thermal equilibrium between the gas and the cavity. A typical measurement result of the sensor temperatures, as illustrated in fig. S3, shows the temperature drift of the two sensors over a period of 7.5 hours. The results indicate fluctuations of less than 2 mK, with a temperature difference of approximately 2 mK between the two sensors. The

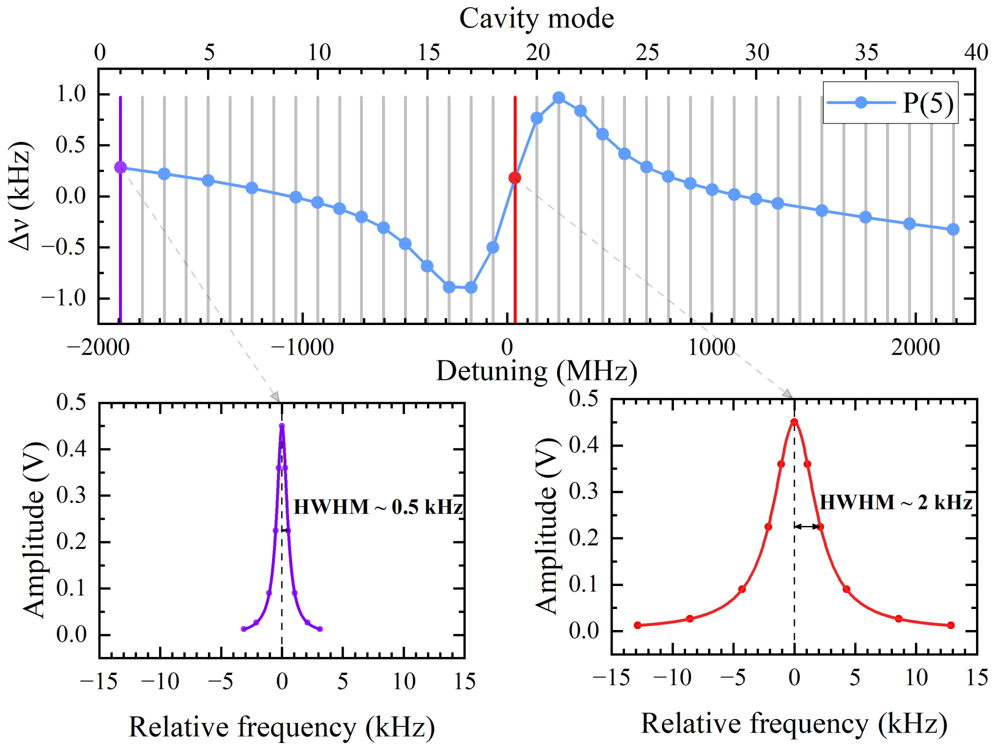

Figure S2: **Single demonstration of the CMDS spectrum.** Transmitted laser amplitude spectra at two different cavity modes (lower panels). The difference between the center frequencies with/without gas, $\Delta\nu$ of each cavity mode, was determined, which contributes to the CMDS spectrum shown in the upper panel.

experimental temperature value was determined by averaging the readings from both sensors.

Gas pressure was measured using a diaphragm pressure gauge (Leybold CTR101N, range 10 Torr) with a nominal uncertainty of 1.2‰. Given the wide range of line strengths, the sample pressure during the experiments varied between 3 Pa and 648 Pa, depending on the intensity of the spectral lines being measured.

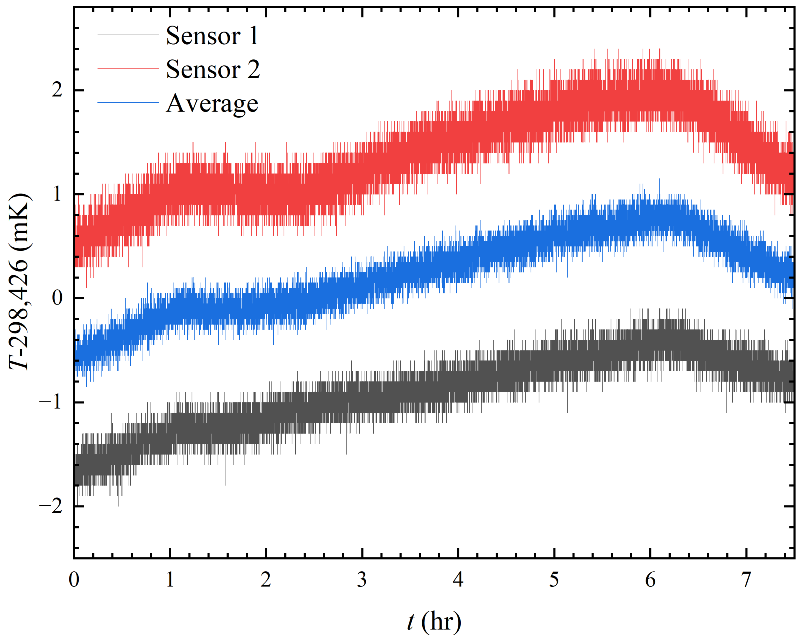

Figure S3: **Temperature drift of the sample cavity monitored by platinum sensors.** The red and grey lines illustrate the temperature drift plots derived from each of the two sensors within the sample chamber across a span of 7.5 hours. Meanwhile, the blue line depicts the average temperature outcome from both sensors.

In principle, the all-frequency-based CMDS method is irrelevant to mirror reflectivities. However, HR mirrors are essential because they ensure a narrow cavity mode width, enabling precise determination of the mode center frequency. Additionally, the mode width must be sufficiently narrow compared to the molecular linewidth, as the dispersion signal measured at a given mode represents an average over the mode's frequency range. In our setup, the cavity mode width remains below 2 kHz across the entire measurement range, while the Doppler-broadened molecular linewidth exceeds 200 MHz. This large disparity (mode width $\ll$ molecular linewidth) means that minor changes in mirror reflectivity, as long as they maintain a sufficiently high reflectivity to preserve the narrow mode width, have a negligible impact. Particularly, the reflectivities at the two wavelengths do not need to be matched; they only need to ensure that the cavity modes remain sharp enough for accurate frequency determination.

Line-intensity ratios and uncertainties

The dispersion spectra can be expressed as follows:

$$\frac{\Delta\tilde{\nu}}{\tilde{\nu}_M} = \frac{I}{2n\tilde{\nu}_C} \times \mathrm{Im}[\varphi(\tilde{\nu}_M - \tilde{\nu}_C)], \tag{S3}$$

where $\tilde{\nu}_M$ is the $M - th$ mode frequency of the cavity, $\tilde{\nu}_C$ is the center frequency of the transition, I is the area under the absorption line (amplitude), and n is the refractive index. The profile of the dispersion spectrum is the imaginary component of the normalized line function $\varphi(\tilde{\nu_M} - \tilde{\nu}_C)$ (*31*).

Speed-dependent Voigt (SDV) profile was adopted to fit the experimental spectra. The SDV profile parameters include: the line center frequency ν_C, the integrated absorption area I, the Doppler half-width Γ_D, the Lorentzian half-width Γ_0, the speed-dependent collisional narrowing coefficient Γ_2, the pressure shift coefficient Δ_0, and the speed-dependent pressure shift coefficient Δ_2.

During the fitting process, ν_C and I were treated as free parameters. The Doppler half-width Γ_D was fixed to the calculated value at the experimental temperature, while Γ_0 and Γ_2 were fixed as the product of the experimental pressure and the parameters γ_0 and γ_2. The pressure shift coefficients Δ_0 and Δ_2 were set to zero. The obtained intensity ratios and their statistical uncertainties are listed in table S1 (column 4).

The uncertainties in the experimentally measured intensity ratios primarily arise from the statistical uncertainty, temperature fluctuations, frequency drift, and spectral fitting methods.

Statistical Errors: The intensity ratio data were derived from fitting over 600 spectra for each pair of lines. The statistical uncertainty for each intensity ratio was approximately 4×10^{-5}, as shown in table S1. For some line pairs, multiple measurements were conducted under different conditions, and the results are also listed in the same table. These results are consistent within the error margins.

Line Profile Parameters: When fitting the spectral data with the SDV profile, attempts were made to either fix or free the parameters Γ_0 and Γ_2. The relative deviation in the intensity ratios obtained from these fits was less than 45 ppm, which is comparable to the statistical uncertainty.

Frequency Calibration: The frequency of the RF signal used to tune the f-EOM sidebands for scanning the dispersion spectra was referenced to a GPS-calibrated rubidium clock, with a nominal uncertainty of 2×10^{-12}. The precision of the microwave frequency was better than 0.01 Hz, making its contribution to the experimental error negligible.

Temperature Drift: During measurements, the temperature drift of the system was typically around 1 mK. For all measured line pairs, the energy difference between the lower states $|E_1 - E_2|$ did not exceed 160 cm^{-1}. According to Eq. S5 (see below), the contribution of temperature drift to the intensity ratio was less than 1×10^{-5}.

Table S1: Line-intensity ratios of CO lines in the (3-0) band. Uncertainties in parentheses are 1σ statistical errors.

Transition	P (Pa)	T (K)	I_1/I_2 at T_{exp} [1]			$A(m_1)/A(m_2)$ [2]		
			Exp.	**UCL2025**	**UCL2022**	**Exp.**	**UCL2025**	**UCL2022**
R(0) / R(1)	15.88	298.429	0.503012(20)	0.503034	0.503053	0.822015	0.822050	0.822082
R(1) / R(3)	8.14	298.430	0.534955(15)	0.534964	0.535003	0.875766	0.875781	0.875845
R(3) / R(5)	6.95	298.426	0.767994(18)	0.768060	0.768112	0.936956	0.937037	0.937100
R(5) / R(10)	7.12	298.431	1.073886(17)	1.073925	1.074081	0.901332	0.901365	0.901496
R(1) / R(10)	7.18	298.431	0.441206(10)	0.441258	0.441384	0.739608	0.739695	0.739907
R(10) / R(13)	7.18	298.430	1.472357(19)	1.472480	1.472584	0.950862	0.950942	0.951009
R(13) / R(15)	7.18	298.429	1.458483(58)	1.458540	1.458599	0.968856	0.968894	0.968933
R(15) / R(17)	14.33	298.426	1.594931(48)	1.595013	1.595069	0.969778	0.969828	0.969862
R(17) / R(19)	26.12	298.430	1.738204(35)	1.738285	1.738336	0.970451	0.970496	0.970524
R(19) / R(21)	50.62	298.430	1.889597(38)	1.889763	1.889809	0.970908	0.970993	0.971017
R(21) / R(22)	50.62	298.432	1.417658(30)	1.417585	1.417600	0.985592	0.985542	0.985552
R(22) / R(23)	98.36	298.434	1.446427(52)	1.446543	1.446556	0.985549	0.985628	0.985637
R(23) / R(24)	98.36	298.437	1.475842(22)	1.475839	1.475850	0.985708	0.985706	0.985713
R(24) / R(25)	206.0	298.434	1.505442(45)	1.505511	1.505520	0.985731	0.985776	0.985782
R(25) / R(26)	422.2	298.429	1.535529(49)	1.535573	1.535581	0.985812	0.985840	0.985845
R(26) / R(27)	423.9	298.428	1.566004(63)	1.566029	1.566035	0.985883	0.985899	0.985902
R(1) / P(1)	12.88	298.428	2.076074(125)	2.076108	2.075855	0.416684	0.416691	0.416640
R(5) / P(5)	3.29	298.430	1.376124(28)	1.376060	1.375445	0.965122	0.965077	0.964646
	7.58	298.429	1.376132(41)			0.965128		
	11.21	298.928	1.376095(43)			0.965102		
R(10) / P(10)	6.42	298.428	1.428264(49)	1.428260	1.427033	1.209416	1.209413	1.208373
R(15) / P(15)	12.88	298.428	1.567518(47)	1.567575	1.565564	1.428752	1.428804	1.426971
R(17) / P(17)	12.88	298.427	1.634831(65)	1.634820	1.632438	1.519477	1.519466	1.517252
R(20) / P(20)	49.12	298.428	1.745511(70)	1.745488	1.742478	1.661507	1.661486	1.658621
R(21) / P(21)	49.12	298.427	1.784819(93)	1.784836	1.781596	1.710702	1.710718	1.707613

Continued on next page

Table S1 – Continued

Transition	P (Pa)	T (K)	I_1/I_2 at T_{exp} [1]			$A(m_1)/A(m_2)$ [2]		
			Exp.	**UCL2025**	**UCL2022**	**Exp.**	**UCL2025**	**UCL2022**
	77.07	298.430	1.784829(36)			1.710712		
	97.11	298.428	1.784802(45)			1.710686		
R(23) / P(23)	121.8	298.431	1.867087(56)	1.867108	1.863374	1.812346	1.812367	1.808742
	125.7	298.427	1.867099(75)			1.812358		
	139.6	298.427	1.867157(50)			1.812414		
	153.5	298.429	1.867182(56)			1.812439		
R(26) / P(26)	225.8	298.427	1.999426(130)	1.999373	1.994801	1.973568	1.973515	1.969003
	334.6	298.428	1.999467(80)			1.973609		
	417.6	298.431	1.999478(99)			1.973620		
	440.7	298.428	1.999611(64)			1.973751		
	529.8	298.429	1.999612(52)			1.973752		
	543.5	298.428	1.999598(56)			1.973738		
	647.6	298.427	1.999587(56)			1.973727		

[1] I_1/I_2 corresponds to the line intensity ratio between two transitions at the experimental temperature;

[2] $A(m_1)/A(m_2)$ corresponds to the ratio of Einstein-A coefficients of two transitions.

S2 Empirical model

Einstein-A coefficients

The intensity of a rovibrational transition at temperature T, which can be experimentally determined as the integrated absorbance divided by the molecular number density, is given by (*34, 35*):

$$S = \frac{n_a g' A}{8\pi c\tilde{\nu}^2 Q(T)} \exp(-\frac{E}{k_B T})[1 - \exp(-\frac{hc\tilde{\nu}}{k_B T})], \tag{S4}$$

where h is the Planck constant, c is the speed of light, k_B is the Boltzmann constant, n_a is the isotopologue abundance, g' is the statistical weights of the upper state, A is the Einstein-A

coefficient, $Q(T)$ is the partition function (*36*), $\tilde{\nu}$ is the transition frequency in wavenumber, and E is the lower-state energy.

Therefore, the experimentally measured line-intensity ratio of two lines relates to the ratio of their Einstein-A coefficients:

$$\frac{S_1(m_1,T)}{S_2(m_2,T)} = \frac{\tilde{\nu}_2^2 g_1' A_1}{\tilde{\nu}_1^2 g_2' A_2} \exp(\frac{E_2 - E_1}{k_B T}) \frac{1 - e^{-\frac{hc\tilde{\nu}_1}{k_B T}}}{1 - e^{-\frac{hc\tilde{\nu}_2}{k_B T}}}. \tag{S5}$$

The intensity ratio between $S_1(m_1,T)$ and $S_2(m_2,T)$ can be directly inferred from the integrated area ratio of the lines I_1 and I_2, determined through experimental spectrum fitting. In the case of the rotation-vibration transitions of CO, the g' factor is expressed as $2J' + 1$, with J' representing the rotational quantum number of the upper state. For two near-infrared transitions ($hc\tilde{\nu} \gg k_BT$), the value of the term $\exp(-\frac{hc\tilde{\nu}}{k_BT})$ is exceedingly small ($\ll 10^{-10}$), and therefore negligible. Einstein-A ratios were derived according to Eq. S5, and they are listed in table S1.

The main source of error in the Einstein-A ratio comes from the experimental line intensity ratio and the temperature uncertainty when employing Eq. S5. Errors related to transition frequency and lower state energy levels are negligible. As stated earlier, temperature measurement uncertainties were predominantly due to probe calibration error of 5 mK. For each analyzed line pair, the difference in lower state energy levels, $|E_1 - E_2|$, was chosen below 160 cm^{-1}. The relative uncertainty from temperature errors was calculated to be below 1.6×10^{-5} according to Eq. S5. Note that for a line pair sharing the same lower state, the R(J)/P(J) ratio is temperature-independent.

In order to ensure consistency, separate measurements were taken for the intensity ratios of the following three pairs of spectral lines: R(1) to R(3), R(3) to R(5), and R(5) to R(10). Based on table S1, one can compute that $\frac{A_{R(1)}}{A_{R(3)}} \times \frac{A_{R(3)}}{A_{R(5)}} \times \frac{A_{R(5)}}{A_{R(10)}} = 0.875765(25) \times 0.936955(22) \times 0.901324(18) = 0.739584(31)$. Furthermore, a separate measurement was conducted for the intensity ratio between R(1) and R(10), yielding $\frac{A_{R(1)}}{A_{R(10)}} = 0.739599(21)$. The results demonstrate an excellent agreement within the allowable margin of error.

Herman-Wallis Factors

In the context of diatomic molecules, the Einstein-A coefficient can be expressed as the product of the vibrational transition dipole moment component, a rotational component known as the

Hönl-London factor describing the dependence of spectroscopic line intensities on the rotational quantum number, and a correction factor known as the Herman-Wallis factor (HWF) associated with vibration-rotation coupling (*35, 57, 58*). Therefore, the Einstein-A coefficient of a specific rovibrational transition can be interpreted as:

$$A = \frac{16\pi^3 \tilde{\nu}^3}{3\epsilon_0 h(2J' + 1)} |\mathbf{M}_{vib}|^2 \mathcal{L} F(m), \tag{S6}$$

where $\mathbf{M}_{vib}$ is the vibrational transition dipole moment independent of rotation quantum numbers, the rotational quantum number m is defined as $J + 1$ for an R branch line and $-J$ for a P branch line, and $\mathcal{L}$ is the Hönl-London factor. For rovibrational transitions of CO, we have $\mathcal{L}_{P(J)} = J$ and $\mathcal{L}_{R(J)} = J + 1$. The Herman-Wallis factor can be expressed as $F(m) = (1 + Cm + Dm^2 + \cdots)^2$. Therefore, the Einstein-A ratio of two infrared transition lines of CO in the same vibrational band can be converted to the ratios of HWFs:

$$\frac{A_1}{A_2} = \frac{\tilde{\nu}_1^3 (2J_2' + 1)\mathcal{L}_{m_1}}{\tilde{\nu}_2^3 (2J_1' + 1)\mathcal{L}_{m_2}} \times \frac{F_{m_1}}{F_{m_2}}. \tag{S7}$$

As shown in fig. S4, we applied second- and third-order polynomial fit within the HWF model to the experimental data, and the obtained HWF parameters are as follows:

$$F^{(2)}(m) = (1 + \frac{m}{168.3252} + \frac{m^2}{35204})^2, \tag{S8}$$

$$F^{(3)}(m) = (1 + \frac{m}{169.0628} + \frac{m^2}{30966} + \frac{m^3}{16883000})^2. \tag{S9}$$

To facilitate comparing the results, we used the R(15) line as a reference to normalize the values of other lines. For example, the R(1)/R(15) ratio was derived as follows: R(1)/R(15) = R(1)/R(3) × R(3)/R(5) × R(5)/R(10) × R(10)/R(15). For the P(J) data, the R(J)/R(15) value and the R(J)/P(J) ratio were used. Note the accumulation of experimental errors during such a transfer process. The ratios of Einstein-A ratios, derived from Eqs. S8& S9, are presented by table S2. We can see that the third-order polynomial model (Eq. S9) can reproduce well the experimental values. The statistical deviation is approximately 2.4×10^{-5}, being comparable with the experimental uncertainties. The second-order polynomial fitting results (Eq.. S8) have a deviation of 1.9×10^{-3}. The deviations between the ratios of $F(m)/F(16)$ obtained from different models are shown in fig. S4C. All results are illustrated as deviations from those given by Eg. S9. The experimental results are also presented

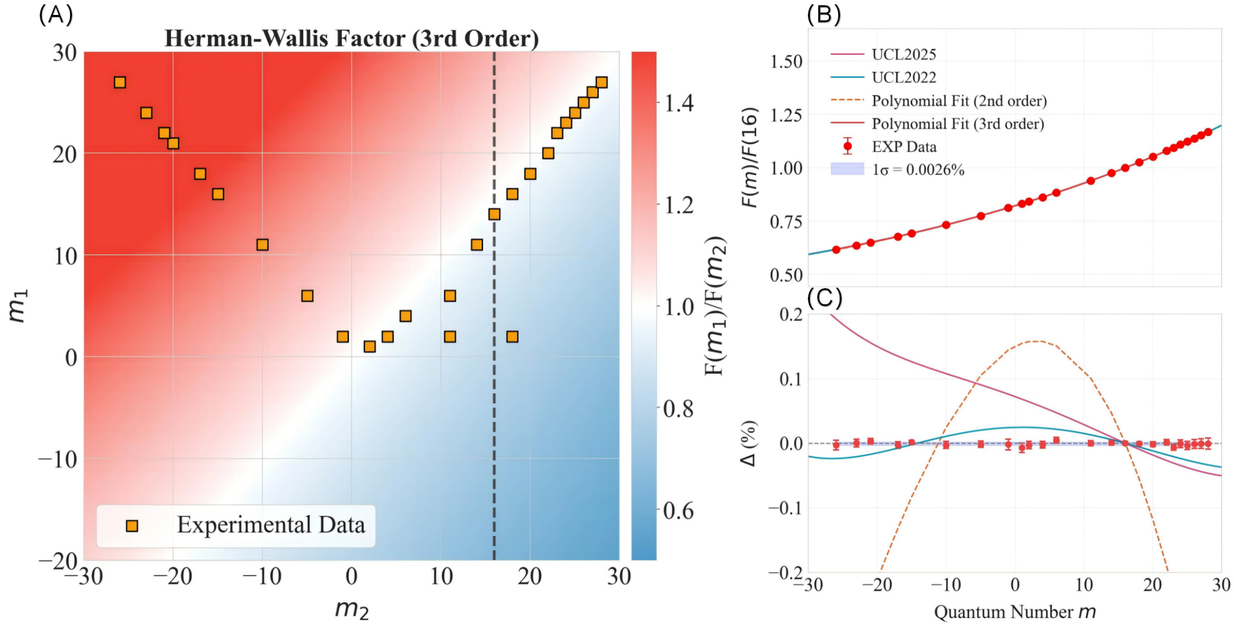

Figure S4: **The Herman-Wallis factors (HWFs) for the (3-0) band of ^{12}C^{16}O.** (A) Ratios of HWFs, $F(m_1)/F(m_2)$, representing values according to Eq. S9. Experimental data points are indicated as orange squares. The dashed line marks $m_2 = 16$. (B) Ratios of HWFs referenced to the R(15) line, $F(m_1)/F(16)$, representing the data along the dashed line marked on the panel (A), see the *Supporting Information*. Red dots show the experimental values. Blue and pink curves are the UCL2025 and UCL2022 *ab initio* calculated results, respectively. The red solid and dashed lines represent the analytical results given by Eq. S9. (C) The relative deviations $\Delta = \delta_{F(m)/F(16)}/\delta^{fit}_{F(m)/F(16)} - 1$(in %) of the UCL2022 and UCL2025 results against the empirical model from the analytical results of Eq. S9. The orange dashed line indicates the analytical result obtained by a 2nd-order polynomial fit to the experimental results. The gray-blue shadow indicates the ±σ confidence region.

as scattering points in the figure. We can see that the experimental results are well reproduced by Eq. S9 including the third-order term. If a Herman-Wallis type function limited to the second-order term is used, the deviation (orange dashed line on fig. S4) reaches over 0.1% for most lines. The *ab initio* results (*7*) have an almost linear deviation, indicating a distinct difference in the P and R branches. As a result, the *ab initio* calculated R(J)/P(J) line intensity ratios show a considerable J-dependent deviation from the experimental results.

The conventional Herman-Wallis factor model incorporates only first-order and second-order terms. However, in high-precision experimental studies or high rotational quantum number (J) transitions, the contributions from vibrational anharmonicity, centrifugal distortion effects, and higher-order derivatives of the dipole moment become non-negligible. Under such conditions, a third-order correction term (e.g., m^3) must be incorporated to enhance the model's predictive accuracy. Including the third-order coefficient signifies a refined characterization of the vibration-rotation interaction on the matrix elements of dipole moments of diatomic molecules. This refinement is fundamentally rooted in three physical phenomena: (1) the intrinsic higher-order anharmonicity of nuclear motion (manifested through asymmetric potential energy surface deformations), (2) energy redistribution between rotational and vibrational modes (mediated by Coriolis coupling and centrifugal distortion), and (3) nonlinear dipole moment responses to nuclear displacement, quantified through the third-order term μ_3 in the Taylor expansion of the dipole moment function $\mu(R)$.

S3 *Ab initio* Calculations

The interaction and complementary mutual validation of experiment and theory is the constant feature of high-accuracy line intensity studies. It is only through such close interaction that new and subtle characteristics can be discovered. The ability to conduct intensity ratio measurements an order of magnitude more accurately than the absolute line intensities shines a new light on theoretical approaches.

The traditional model for high accuracy transitions intensities of a vibrational band relies on a single "band" transition dipole with the behavior on individual line intensities as a function of J accounted for by analytic Hönl-London factors; corrections due to small variations in the wavefunction caused by vibration-rotation interactions are then modeled using empirical Hermann-Wallis

Table S2: The Herman-Wallis factors (HWFs) of the corresponding transitions normalized to the R(15) line in the (3-0) band of CO.

Trans.	Exp.	Fit (P2)	Fit (P3)	UCL2025		UCL2022	
				Value	Δ (%)	Value	Δ (%)
P(26)	0.617673	0.615390	0.617690	0.617575	-0.0186	0.618912	0.1978
P(23)	0.636816	0.634967	0.636812	0.636702	-0.0173	0.637909	0.1723
P(21)	0.650156	0.648604	0.650134	0.650038	-0.0148	0.651162	0.1581
P(17)	0.678199	0.677329	0.678218	0.678172	-0.0068	0.679138	0.1356
P(15)	0.693021	0.692440	0.693011	0.692996	-0.0022	0.693886	0.1263
P(10)	0.732290	0.732489	0.732309	0.732376	0.0091	0.733087	0.1062
P(5)	0.775116	0.775932	0.775124	0.775262	0.0178	0.775807	0.0881
P(1)	0.812081	0.813259	0.812095	0.812269	0.0214	0.812690	0.0733
R(0)	0.831480	0.832816	0.831538	0.831720	0.0219	0.832083	0.0655
R(1)	0.841483	0.842824	0.841507	0.841691	0.0219	0.842025	0.0616
R(3)	0.861937	0.863306	0.861955	0.862135	0.0209	0.862414	0.0533
R(5)	0.883138	0.884421	0.883097	0.883267	0.0193	0.883493	0.0448
R(10)	0.939136	0.940074	0.939136	0.939243	0.0114	0.939347	0.0225
R(13)	0.975065	0.975502	0.975052	0.975100	0.0049	0.975139	0.0089
R(15)	1.000000	1.000000	1.000000	1.000000	—	1.000000	—
R(17)	1.025775	1.025219	1.025779	1.025727	-0.0051	1.025691	-0.0086
R(19)	1.052400	1.051175	1.052415	1.052306	-0.0104	1.052238	-0.0168
R(21)	1.079951	1.077884	1.079932	1.079765	-0.0155	1.079669	-0.0244
R(22)	1.093962	1.091525	1.094029	1.093834	-0.0178	1.093725	-0.0278
R(23)	1.108349	1.105361	1.108357	1.108133	-0.0202	1.108014	-0.0309
R(24)	1.122880	1.119393	1.122918	1.122667	-0.0224	1.122537	-0.0339
R(25)	1.137704	1.133623	1.137716	1.137439	-0.0243	1.137301	-0.0365
R(26)	1.152752	1.148053	1.152755	1.152454	-0.0261	1.152308	-0.0388
R(27)	1.168031	1.162686	1.168038	1.167714	-0.0277	1.167562	-0.0408

[*] Fit(P2) and Fit(P3) correspond to quadratic and cubic polynomial expansions of $F(m)$;

[†] Δ is the relative deviation of the calculated value from the Fit(P3) value given by Eq. S9, in %.

factors. Our first principles approach uses the precise, rotational-state dependent wavefunctions obtained by direct and accurate solution of the nuclear-motion Schrödinger equation (*59*); these solutions have been demonstrated to be highly accurate (*60*), and this approach to more robust than using even empirically determined Hermann-Wallis factors (*12*). Instead of using a single transition dipole our approach uses a dipole moment curve (DMC) which varies as a function of internuclear separation. These curves are computed using state-of-the-art high-level *ab initio* theory. *Ab initio* electronic structure theory is largely concerned with obtaining good energy predictions and, in particular, the use of variational methods which ensure that larger calculations yield a better (lower) energy. However, dipoles are not subject to the variational principle; their calculation relies on obtaining a balanced treatment of the problem, which, for CO, means that the calculation treats the electronic charge distribution about each atom at precisely the same level. Our cited studies and this work show that is the *ab initio* treatment of the dipole moment which is the key to obtaining ultra-high accuracy.

All electronic structure computations were carried out with the quantum chemistry package Molpro (*61*). Dipoles were computed using the finite differences (FD) approach, which necessitated two calculations per point for the dipoles and one other at zero field to obtain the energy at that geometry (*62*).

Dipoles were calculated at the multi-reference configuration interaction (MRCI) level of theory, the fixed reference Davidson correction (+Q) has been applied to the MRCI dipoles using aug-cc-pCV6Z basis set (*61*). We note that extensive coupled-cluster calculations by Koput (*63*) gave CO transition intensities significantly less accurate than our previous MRCI studies. At the MRCI level, the accuracy of the DMC is largely determined by the complete active space (CAS) employed, here 6220. In order to calculate the CO line intensities one variationally we used the Duo program (*59*), which solves the rovibrational Schrödinger equation with the use of DMC described above, and the potential energy curve (PEC) taken from Ref. (*64*). This approach is fully within the Born-Oppenheimer approximation; one correction to which is rotational non-adiabatic contribution as represented by the J-dependent effective potential of Meshkov *et al.* (*27*) We plan to study the effects of Born-Oppenheimer breakdown in its entirety in future work.

A comparison of line intensity ratios obtained using accurate *ab initio* dipole moments calculations (UCL2022) (*7*) is presented in table S1. However, the calculated results of the ratios R(J)/P(J),

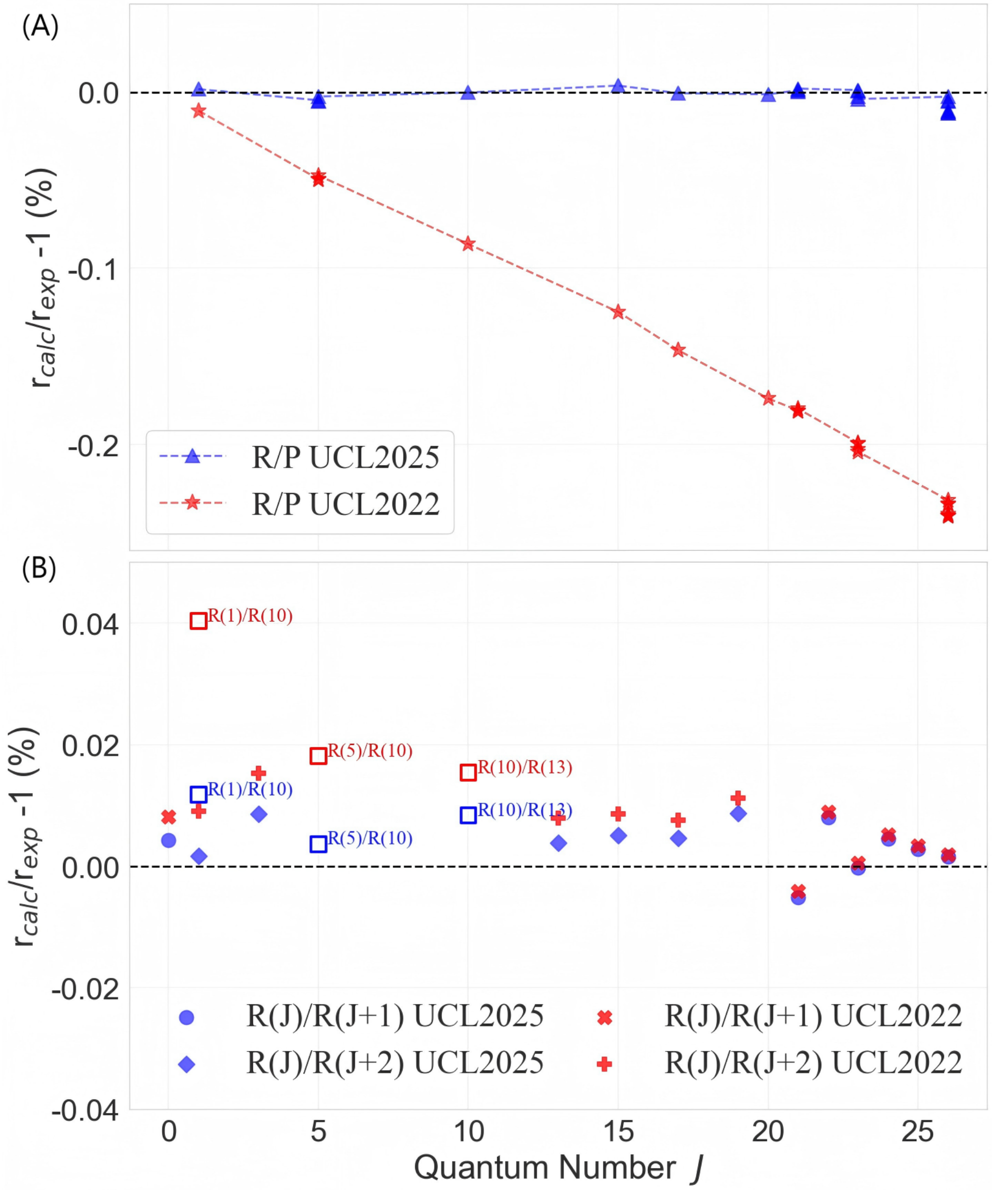

Figure S5: **Comparison with theoretical calculations.** Discrepancies between observed line-intensity ratios and ab initio calculated results from this work, designated as UCL2025, and the previous calculated results (*7*), noted as UCL2022. (A) Intensity ratios of R(J)/P(J) pairs. (B) Discrepancies between the calculated and experimental ratios of R(J)/R($J+1$) and R(J)/R($J+2$). Ratios of R(1)/R(10), R(5)/R(10), and R(10)/R(13) are also explicitly marked.

R(J)/R(J + 1), and R(J)/R(J + 2) using UCL2022 are found to lie well outside the experimental uncertainties (see table S1). fig. S4 plots observed minus calculated (obs-calc) residues for the R(J)/P(J) residues, showing that the UCL2022 residues give a straight line at an angle to the J axis. This angle represents a discovery in this work characteristics of the relative line intensities, different from the conventional characteristics of absolute line intensities. Minimization of this angle represents a goal for future theoretical calculation of the R(J)/P(J) or R(J)/R(J + N).

We tested different versions of the dipole moment curves (DMCs *ab initio* calculations developed in Ref. (*7*) and found that a new DMC calculation (UCL2025) using a 6220 Complete Active Space (CAS), as compared to the CAS 7220 used in Ref. (*7*), results in agreement within the experimental uncertainty (see table S1). As shown in fig. S4, the UCL2025 calculations show that the angle of the line is practically zero, which represents excellent agreement between calculations and experiment. The standard deviation of the obs.-calc. residues is 0.003% and the mean value of these residues is only 0.0003%. No characteristics of the line intensities have ever been demonstrated with such an agreement between *ab initio* theory and experiment. As listed in table S1, we compared the results of calculations and observations for two other ratios, R(J)/R(J+1) and R(J)/R(J+2). The standard deviations of the residues are slightly larger, that is, 0.007% for R(J)/R(J + 1) and about 0.006% for R(J)/R(J + 2). The residues given in table S1 are illustrated in fig. S S5. Though the calculated R(J)/R(J + N) ratios agree less well with the experiment, they are still close to the experimental uncertainties. Although the obs.-calc. for ratios between lines with different J are somewhat larger, these measurements could be used for accurate LRT temperature measurement, while the R(J)/P(J) ratios are independent of temperature and cannot be used for this purpose.

REFERENCES AND NOTES

1. D. J. Des Marais, M. O. Harwit, K. W. Jucks, J. F. Kasting, D. N.C. Lin, J. I. Lunine, J. Schneider, S. Seager, W. A. Traub, N. J. Woolf, Remote sensing of planetary properties and biosignatures on extrasolar terrestrial planets. *Astrobiology* **2**, 153–181 (2002).

2. O. L. Polyansky, K. Bielska, M. Ghysels, L. Lodi, N. F. Zobov, J. T. Hodges, J. Tennyson, High-accuracy CO_2 line intensities determined from theory and experiment. *Phys. Rev. Lett.* **114**, 243001 (2015).

3. E. Roueff, H. Abgrall, P. Czachorowski, K. Pachucki, M. Puchalski, J. Komasa, The full infrared spectrum of molecular hydrogen. *Astron. Astrophys.* **630**, A58 (2019).

4. C. W. Bauschlicher Jr., S. R. Langhoff, P. R. Taylor, in *Accurate Quantum Chemical Calculations* (John Wiley & Sons, Ltd., 1990), pp. 103–161.

5. A. J. Fleisher, E. M. Adkins, Z. D. Reed, H. Yi, D. A. Long, H. M. Fleurbaey, J. T. Hodges, Twenty-five-fold reduction in measurement uncertainty for a molecular line intensity. *Phys. Rev. Lett.* **123**, 043001 (2019).

6. H. Tran, C. Boulet, J. Hartmann, Line mixing and collision-induced absorption by oxygen in the A band: Laboratory measurements, model, and tools for atmospheric spectra computations. *J. Geophys. Res. Atmos.* **111**, D15210 (2006).

7. K. Bielska, A. A. Kyuberis, Z. D. Reed, G. Li, A. Cygan, R. Ciuryło, E. M. Adkins, L. Lodi, N. F. Zobov, V. Ebert, D. Lisak, J. T. Hodges, J. Tennyson, O. L. Polyansky, Subpromille measurements and calculations of CO (3-0) overtone line intensities. *Phys. Rev. Lett.* **129**, 043002 (2022).

8. A. A. Balashov, K. Bielska, G. Li, A. A. Kyuberis, S. Wójtewicz, J. Domysławska, R. Ciuryło, N. F. Zobov, D. Lisak, J. Tennyson, O. L. Polyansky, Measurement and calculation of CO (7–0) overtone line intensities. *J. Chem. Phys.* **158**, 234306 (2023).

9. N. F. Zobov, R. I. Ovsyannikov, M. A. Rogov, E. I. Lebedev, J. Tennyson, O. L. Polyansky, CO line intensities: Towards subpercent accuracy of intensities of all bands. *J. Quant. Spectrosc. Radiat. Transf.* **325**, 109510 (2025).

10. J. Komasa, M. Puchalski, P. Czachorowski, G. Lach, K. Pachucki, Rovibrational energy levels of the hydrogen molecule through nonadiabatic perturbation theory. *Phys. Rev. A* **100**, 032519 (2019).

11. M. Puchalski, J. Komasa, P. Czachorowski, K. Pachucki, Nonadiabatic QED correction to the dissociation energy of the hydrogen molecule. *Phys. Rev. Lett.* **122**, 103003 (2019).

12. J. T. Hodges, K. Bielska, M. Birk, R. Guo, G. Li, J. S. Lim, D. Lisak, Z. D. Reed, G. Wagner, International comparison CCQM-P229 pilot study to measure line intensities of selected $^{12}C^{16}O$ transitions. *Metrologia* **62**, 08006 (2025).

13. Q. Huang, Y. Tan, R.H. Yin, Z.L. Nie, J. Wang, S.M. Hu, Line intensities of CO near 1560 nm measured with absorption and dispersion spectroscopy. *Metrologia* **61**, 065003 (2024).

14. H. Fleurbaey, A. Koroleva, S. Kassi, A. Campargue, The high accuracy spectroscopy of H2 rovibrational transitions in the (2-0) band near 1.2 μm. *Phys. Chem. Chem. Phys.* **25**, 14749–14756 (2023).

15. H. Liang, Y. Tan, C.L. Hu, Z.L. Nie, A.W. Liu, Y. R. Sun, J. Wang, S.M. Hu, Cavity-enhanced absorption and dispersion spectroscopy of the 1238-nm line of H_2. *Phys. Rev. A* **110**, 042817 (2024).

16. A. J. Fleisher, H. Yi, A. Srivastava, O. L. Polyansky, N. F. Zobov, J. T. Hodges, Absolute $^{13}C/^{12}C$ isotope amount ratio for Vienna PeeDee Belemnite from infrared absorption spectroscopy. *Nat. Phys.* **17**, 889–893 (2021).

17. M. Aldén, Spatially and temporally resolved laser/optical diagnostics of combustion processes: From fundamentals to practical applications. *Proc. Combust. Inst.* **39**, 1185–1228 (2023).

18. M. Quack, F. Merkt, eds., in *Fundamental Symmetries and Symmetry Violations from High Resolution Spectroscopy* (Wiley, 2011), pp. 659–722.

19. Y. Shimizu, S. Okubo, A. Onae, K. M. T. Yamada, H. Inaba, Molecular gas thermometry on acetylene using dual-comb spectroscopy: Analysis of rotational energy distribution. *Appl. Phys. B* **124**, 71 (2018).

20. R. Gotti, M. Lamperti, D. Gatti, S. Wójtewicz, T. Puppe, Y. Mayzlin, B. Alsaif, J. Robinson-Tait, F. Rohde, R. Wilk, P. Leisching, W.G. Kaenders, P. Laporta, M. Marangoni, Multispectrum rotational states distribution thermometry: Application to the $3\nu_1 + \nu_3$ band of carbon dioxide. *New J. Phys.* **22**, 083071 (2020).

21. L. Santamaria, M. S. D. Cumis, D. Dequal, G. Bianco, C. P. Pablo, A new precision spectroscopy based method for Boltzmann constant determination and primary thermometry. *J. Phys. Chem. A* **122**, 6026–6030 (2018).

22. R. Gotti, M. Lamperti, D. Gatti, M. Marangoni, Laser-based primary thermometry: A review. *J. Phys. Chem. Ref. Data Monogr.* **50**, 031501 (2021).

23. J. Fischer, B. Fellmuth, C. Gaiser, T. Zandt, L. Pitre, F. Sparasci, M.D. Plimmer, M. de Podesta, R. Underwood, G. Sutton, G. Machin, R.M. Gavioso, D. Madonna Ripa, P.P.M. Steur, J. Qu, X.J. Feng, J. Zhang, M.R. Moldover, S.P. Benz, D.R. White, L. Gianfrani, A. Castrillo, L. Moretti, B. Darquié, E. Moufarej, C. Daussy, S. Briaudeau, O. Kozlova, L. Risegari, J.J. Segovia, M.C. Martín, D. del Campo, The Boltzmann project. *Metrologia* **55**, R1–R20 (2018).

24. M. Stock, R. Davis, E. de Mirandés, M. J. T. Milton, The revision of the SI—The result of three decades of progress in metrology. *Metrologia* **56**, 022001 (2019).

25. C. Daussy, M. Guinet, A. Amy-Klein, K. Djerroud, Y. Hermier, S. Briaudeau, C. J. Bordé, C. Chardonnet, Direct determination of the Boltzmann constant by an optical method. *Phys. Rev. Lett.* **98**, 250801 (2007).

26. G. Casa, A. Castrillo, G. Galzerano, R. Wehr, A. Merlone, D. di Serafino, P. Laporta, L. Gianfrani, Primary gas thermometry by means of laser-absorption spectroscopy: Determination of the Boltzmann constant. *Phys. Rev. Lett.* **100**, 200801 (2008).

27. V. V. Meshkov, A. Y. Ermilov, A. V. Stolyarov, E. S. Medvedev, V. G. Ushakov, I. E. Gordon, Semi-empirical dipole moment of carbon monoxide and line lists for all its isotopologues revisited. *J. Quant. Spectrosc. Radiat. Transf.* **280**, 108090 (2022).

28. A. Cygan, S. Wójtewicz, Hubert Jóźwiak, G. Kowzan, N. Stolarczyk, K. Bielska, P. Wcisło, R. Ciuryło, D. Lisak, Dispersive heterodyne cavity ring-down spectroscopy exploiting eigenmode frequencies for high-fidelity measurements. *Sci. Adv.* **11**, eadp8556 (2025).

29. C. F. Cheng, J. Wang, Y. R. Sun, Y. Tan, P. Kang, S.M. Hu, Doppler broadening thermometry based on cavity ring-down spectroscopy. *Metrologia* **52**, S385–S393 (2015).

30. G. Li, A. Röttger, M. Zboril, O. Werhahn, Metrology for climate action. *Meas. Sens.* **38**, 101850 (2025).

31. A. Cygan, P. Wcisło, S. Wójtewicz, P. Masłowski, J. T. Hodges, R. Ciuryło, D. Lisak, One-dimensional frequency-based spectroscopy. *Opt. Expr.* **23**, 14472 (2015).

32. A. Cygan, P. Wcisło, S. Wójtewicz, G. Kowzan, M. Zaborowski, D. Charczun, K. Bielska, R. S. Trawiński, R. Ciuryło, P. Masłowski, D. Lisak, High-accuracy and wide dynamic range frequency-based dispersion spectroscopy in an optical cavity. *Opt. Expr.* **27**, 21810–21821 (2019).

33. J. Wang, Y. R. Sun, L.-G. Tao, A.-W. Liu, S.-M. Hu, Communication: Molecular near-infrared transitions determined with sub-kHz accuracy. *J. Chem. Phys.* **147**, 091103 (2017).

34. M. Šimečková, D. Jacquemart, L. S. Rothman, R. Gamache, A. Goldman, Einstein A-coefficients and statistical weights for molecular absorption transitions in the HITRAN database. *J. Quant. Spectrosc. Radiat. Transf.* **98**, 130–155 (2006).

35. P. F. Bernath, *Spectra of Atoms and Molecules* (Oxford Univ. Press, 2016).

36. R. R. Gamache, B. Vispoel, M. Rey, A. Nikitin, V. Tyuterev, O. Egorov, I. E. Gordon, V. Boudon, Total internal partition sums for the HITRAN2020 database. *J. Quant. Spectrosc. Radiat. Transf.* **271**, 107713 (2021).

37. J. Wang, C.L. Hu, A.W. Liu, Y.R. Sun, Y. Tan, S.M. Hu, Saturated absorption spectroscopy near 1.57 μm and revised rotational line list of $^{12}C^{16}O$. *J. Quant. Spectrosc. Radiat. Transf.* **270**, 107717 (2021).

38. M. R. Moldover, J. P. M. Trusler, T. J. Edwards, J. B. Mehl, R. S. Davis, Measurement of the universal gas constant R using a spherical acoustic resonatore. *J. Res. Natl. Bur. Stand.* **93**, 85–144 (1988).

39. R. M. Gavioso, D. Madonna Ripa, P. P. M. Steur, C. Gaiser, D. Truong, C. Guianvarc'h, P. Tarizzo, F. M. Stuart, R. Dematteis, A determination of the molar gas constant R by acoustic thermometry in helium. *Metrologia* **52**, S274–S304 (2015).

40. L. Pitre, F. Sparasci, L. Risegari, C. Guianvarc'h, C. Martin, M. E. Himbert, M. D. Plimmer, A. Allard, B. Marty, P. A. Giuliano Albo, B. Gao, M. R. Moldover, J. B. Mehl, New measurement of the Boltzmann constant *k* by acoustic thermometry of helium-4 gas. *Metrologia* **54**, 856–873 (2017).

41. X. J. Feng, J. T. Zhang, H. Lin, K. A. Gillis, J. B. Mehl, M. R. Moldover, K. Zhang, Y. N. Duan, Determination of the Boltzmann constant with cylindrical acoustic gas thermometry: New and previous results combined. *Metrologia* **54**, 748–762 (2017).

42. J. J. Segovia, D. Lozano-Martín, M. C. Martín, C. R. Chamorro, M. A. Villamañán, E. Pérez, C. García Izquierdo, D. del Campo, Updated determination of the molar gas constant R by acoustic measurements in argon at UVa-CEM. *Metrologia* **54**, 663–673 (2017).

43. M. de Podesta, D. F. Mark, R. C. Dymock, R. Underwood, T. Bacquart, G. Sutton, S. Davidson, G. Machin, Re-estimation of argon isotope ratios leading to a revised estimate of the Boltzmann constant. *Metrologia* **54**, 683–692 (2017).

44. C. Gaiser, B. Fellmuth, N. Haft, A. Kuhn, B. Thiele-Krivoi, T. Zandt, J. Fischer, O. Jusko, W. Sabuga, Final determination of the Boltzmann constant by dielectric-constant gas thermometry. *Metrologia* **54**, 280–289 (2017).

45. J. Qu, S.P. Benz, K. Coakley, H. Rogalla, W.L. Tew, R. White, K. Zhou, Z. Zhou, An improved electronic determination of the Boltzmann constant by Johnson noise thermometry. *Metrologia* **54**, 549–558 (2017).

46. E. Fasci, M. Domenica de Vizia, A. Merlone, L. Moretti, A. Castrillo, L. Gianfrani, The Boltzmann constant from the $H_2{}^{18}O$ vibration-rotation spectrum: Complementary tests and revised uncertainty budget. *Metrologia* **52**, S233–S241 (2015).

47. A. Castrillo, E. Fasci, H. Dinesan, S. Gravina, L. Moretti, L. Gianfrani, Optical determination of thermodynamic temperatures from a C_2H_2 line-doublet in the near infrared. *Phys. Rev. Appl.* **11**, 064060 (2019).

48. C. Lemarchand, K. Djerroud, B. Darquié, O. Lopez, A. Amy-Klein, C. Chardonnet, C.J. Bordé, S. Briaudeau, C. Daussy, Determination of the Boltzmann constant by laser spectroscopy as a basis for future measurements of the thermodynamic temperature. *Int. J. Thermophys.* **31**, 1347–1359 (2010).

49. L. Moretti, A. Castrillo, E. Fasci, M.D. de Vizia, G. Casa, G. Galzerano, A. Merlone, P. Laporta, L. Gianfrani, Determination of the Boltzmann constant by means of precision measurements of $H_2^{18}O$ line shapes at 1.39 μm. *Phys. Rev. Lett.* **111**, 060803 (2013).

50. K. M. T. Yamada, A. Onae, F.-L. Hong, H. Inaba, T. Shimizu, Precise determination of the Doppler width of a rovibrational absorption line using a comb-locked diode laser. *C. R. Phys.* **10**, 907–915 (2009).

51. R. Hashemi, C. Povey, M. Derksen, H. Naseri, J. Garber, A. Predoi-Cross, Doppler broadening thermometry of acetylene and accurate measurement of the Boltzmann constant. *J. Chem. Phys.* **141**, 214201 (2014).

52. G. W. Truong, E. F. May, T. M. Stace, A. N. Luiten, Quantitative atomic spectroscopy for primary thermometry. *Phys. Rev. A* **83**, 033805 (2011).

53. G. W. Truong, D. Stuart, J. D. Anstie, E. F. May, T. M. Stace, A. N. Luiten, Atomic spectroscopy for primary thermometry. *Metrologia* **52** (5), S324–S342 (2015).

54. R. Gotti, L. Moretti, D. Gatti, A. Castrillo, G. Galzerano, P. Laporta, L. Gianfrani, M. Marangoni, Cavity-ring-down Doppler-broadening primary thermometry. *Phys. Rev. A* **97**, 012512 (2018).

55. D. Lisak, V. D'Agostino, S. Wójtewicz, A. Cygan, M. Gibas, P. Wcisło, R. Ciuryło, K. Bielska, Leveraging resonant frequencies of an optical cavity for spectroscopic measurement of gas temperature and concentration. arXiv:2502.17660 [physics.optics] (2025).

56. G. Galzerano, Absolute temperature measurements by direct-frequency-comb spectroscopy. *Measurement* **164**, 107940 (2020).

57. R. Herman, R. F. Wallis, Influence of vibration-rotation interaction on line intensities in vibration-rotation bands of diatomic molecules. *J. Chem. Phys.* **23** (4), 637–646 (1955).

58. J. K. Watson, Quadratic Herman-Wallis factors in the fundamental bands of linear molecules. *J. Mol. Spectrosc.* **125**, 428–441 (1987).

59. S. N. Yurchenko, L. Lodi, J. Tennyson, A. V. Stolyarov, Duo: A general program for calculating spectra of diatomic molecules. *Comput. Phys. Commun.* **202**, 262–275 (2016).

60. I. I. Mizus, L. Lodi, J. Tennyson, N. F. Zobov, O. L. Polyansky, An analysis of the accuracy of line intensities calculations using DUO and LEVEL program package. *J. Mol. Spectrosc.* **368**, 111621 (2022).

61. H.-J. Werner, P. J. Knowles, G. Knizia, F. R. Manby, M. Schütz, Molpro: A general-purpose quantum chemistry program package. *WIREs Comput. Mol. Sci.* **2**, 242–253 (2012).

62. L. Lodi, J. Tennyson, Theoretical methods for small-molecule ro-vibrational spectroscopy. *J. Phys. B At. Mol. Opt. Phys.* **43**, 133001 (2010).

63. J. Koput, Toward accurate ab initio ground-state potential energy and 2 electric dipole moment functions of carbon monoxide. *J. Chem. Theo. Comput.* **20**, 9041–9047 (2024).

64. J. A. Coxon, P. G. Hajigeorgiou, Direct potential fit analysis of the $X^1\Sigma^+$ ground state of CO. *J. Chem. Phys.* **121**, 2992–3008 (2004).